The UK silicon photonics project

G. Reed, N. Wright, G. Mashanovich, B. Timotijevic, T. Krauss, et al.

G. T. Reed, N. Wright, G. Z. Mashanovich, B. Timotijevic, T. F. Krauss, T. P. White, L. O'Faolain, R. W. Kelsall, L. Lever, Z. Ikonic, A. Valvanis, D. Leadley, E. Findlayson, R. M. Jenkins, "The UK silicon photonics project," Proc. SPIE 7719, Silicon Photonics and Photonic Integrated Circuits II, 77190A (17 May 2010); doi: 10.1117/12.858154

SPIE.

Event: SPIE Photonics Europe, 2010, Brussels, Belgium

The UK Silicon Photonics Project

G T Reed*, N Wright*, G Z Mashanovich*, B Timotijevic*, T F Krauss**, T P White**, L O'Faolain, RW Kelsall***, L Lever***, Z Ikonic´***, A Valavanis***,D Leadley****, E Findlayson****, and RM Jenkins*****.

* Department of Electronic Engineering, University of Surrey, Guildford, Surrey, UK GU2 7XH;
** School of Physics and Astronomy, University of St. Andrews, St. Andrews, Fife, KY16 9SS
*** Centre for Molecular Nanoscience, The University of Leeds, Leeds,
LS2 9JT, UK
**** Department of Physics, University of Warwick, Coventry, CV4 7AL
*****Malvern Technology Centre, St.Andrews Road, Malvern, Worcestershire., UK, WR14 3PS

1. Introduction

The project is a consortium based activity involving researchers from the UK institutions of the Universities of Surrey, St. Andrews, Leeds, Warwick, and Southampton, as well as the commercial research institution QinetiQ. The aims of the project are to progress the state of the art in Silicon Photonics, in the areas of waveguides, modulators, couplers, detectors, Raman processes, and integration with electronics. Thus the field is vast, and impossible to cover comprehensively in one project, nor indeed in one paper. The programme is run on a truly collaborative basis, with members from each institution running one or more work packages within the project, each co-ordinating work from their own plus other institutions. To date, the most well developed work has emerged from the activity on basic waveguides and their characteristics, the modulator activity, optical filters, and work on Raman Amplifiers. This work will be the main focus of this paper, but an attempt will be made to update the audience on the remaining activities within the project. By the nature of the project, much of the work is medium term, and hence some activities are not expected to yield viable results until at least next year, hence the concentration on some activities rather than all activities at this stage.

2. Waveguides

The essential building block of every photonic circuit is the optical waveguide. In this work we analyse influence of oxide stress on the single mode and birefringence free propagation, and also present SOI waveguides fabricated by the Local oxidation of silicon technique. Research and design of the silicon-based photonic integrated circuits (PICs) has been primarily focused on devices optimised for 1.55 μm wavelength, utilised in telecommunications. However, for other applications, such as sensing, imaging or medical applications, wavelengths in the mid-wave- (MWIR) or long-wave infrared (LWIR) spectrum are of interest [1, 2]. As silicon is relatively low loss from 1.2-8 μm and from 24-200 μm [3], a silicon waveguide with air cladding would be also potentially low loss in these two wavelength windows.

2.1 LOCOS waveguides

In order to reduce optical losses in ridge waveguides we have used a well-established VLSI technique of the LOCal Oxidation of Silicon (LOCOS) for waveguide fabrication [4]. By using this approach, waveguides with minimal roughness at the Si/SiO_2 interface can be fabricated, thus reducing the propagation loss. We have fabricated LOCOS waveguides in the sub-micrometer range starting from a p-type material with a 1500nm thick silicon overlayer, and a 2.8μm buried oxide layer. The wafer was thinned using thermal oxidation and subsequently etched in buffered HF to reduce the overlayer thickness to around 700nm. A 40nm SiO_2 layer and a Si_3N_4 masking layer of 80nm was deposited and trenches in the Si_3N_4 layer were then defined by photolithography and plasma etching. The structure was subsequently wet-oxidized to produce a 410nm thick SiO_2 layer in the unmasked trench areas. Finally, the Si_3N_4 layer was removed to leave an optical waveguide between the oxidized trenches [5] (Figure 1).

Silicon Photonics and Photonic Integrated Circuits II, edited by Giancarlo Cesare Righini,
Proc. of SPIE Vol. 7719, 77190A · © 2010 SPIE · CCC code: 0277-786X/10/$18 · doi: 10.1117/12.858154

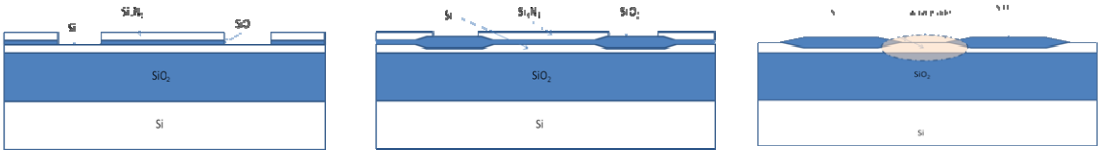

Figure 1. Fabrication of LOCOS waveguides

The typical height of the fabricated waveguides was H=770 nm, the slab height was equal to h=600nm while the sidewall angle was equal to $\theta=27^{o}$. Measured propagation losses at the operating wavelength of 1.55μm for TE polarisation were as low as 0.1dB/cm [5]. We have employed full vectorial complex film mode matching (FMM) technique [6] to analyse the lateral leakage losses in this structure at the operating wavelength of 1.55μm. The main advantage of the mode matching technique over other numerical methods is that the computational window is fully open in the lateral direction, hence the lateral leakage can be modeled accurately.

Propagation losses for the TM mode show exponential behavior and decrease as the waveguide width at the bottom of the rib increases. The main reason for high losses is the polarisation conversion between TM and TE mode and lateral leakage which occurs in shallow etched waveguides [7]. The same theoretical model has been applied in the analysis of a rib waveguide with height equal to H=205nm and etch depth equal to D=15nm, since experimental results for this structure show certain waveguide dimensions at which small losses for TM mode can be achieved [7]. Our theoretical model is in excellent agreement with the experimental data reported by Webster et al. [7]. The oscillations occur at the certain waveguide widths, with a period of 0.72μm, while the first two minima occur at 0.72μm and 1.44μm which was verified by previously reported experimental results [7].

The study of TM-TE mode coupling has been investigated by a number of researchers in the recent years since a number of key sensors and active component designs benefit from TM mode operation [e.g.8, 9]. At the ridge boundaries incident TM mode produces a TE component of the field. Destructive interference occurs at a certain waveguide widths and can be described by the following equation [8, 9]

$$W = \frac{m\lambda}{\sqrt{\left(n_{eff,TE}^{core}\right)^2 - N_{eff,TM}^2}} \quad (1)$$

where W is the waveguide width, m is the positive integer, λ is the operating wavelength, and the last two terms represent the slab effective index of TE mode in the waveguide core and modal effective index of TM mode. The small variation of equation 1 has been recently reported [10] but it gives very small shift (~10nm) in waveguide width at which small losses can be achieved. Figure 2 shows propagation losses for the TM mode for a LOCOS waveguide with H=400nm and variable etch depth and top oxide cover thickness. Due to TE-TM mode conversion at the ridge sidewalls, at certain waveguide widths it is possible to achieve small propagation losses for TM mode. It can be seen that waveguide width of 2.5μm can provide TM mode losses smaller than 0.1dB/cm according to our theoretical model.

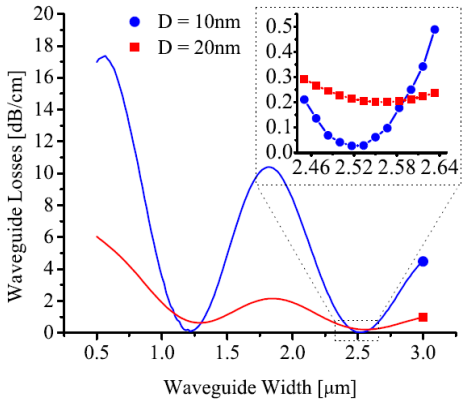

Figure 2. Simulated results for waveguide losses as a function of waveguide width for TM mode (H=400nm, t=2.5D, θ=90°, λ=1.55μm); inset: Enlargement of the results for waveguide widths around W=2.5μm where minimum waveguide losses can be achieved.

2.2 Stress engineering

When designing photonics circuits we need to find dimensions of the waveguides that provide single mode and sometimes also birefringence free propagation ($\Delta N_{eff} = N_{eff}^{TE} - N_{eff}^{TM} = 0$). The oxide cladding causes stress in the waveguide structure, therefore changing the effective refractive indices for TE and TM polarisations due to the photoelastic effect. The total birefringence is the sum of the geometrical birefringence and stress induced birefringence [11].

Figure 3 shows the stress influence on rib waveguide with the height of H=1.35 μm, for an oxide cladding thickness of 1 μm. We assume that the thickness of the upper cladding film on the rib sidewalls is 70% of that on the top. Figure 3(a) represents the waveguide with vertical sidewalls (θ=90°), while Figure 3(b) is for the waveguide with slanted sidewalls (θ=80°). In both figures we present only the quasi-TM mode curves because they define limiting conditions for single-mode behaviour. Conditions for isotropic refractive index of material, and stress-induced effects that produce an anisotropic refractive index distribution in the material are considered. There are three important things that can be seen in Figure 3(a). First, the large difference between the zero birefringence (ZBR) curves shows that stress-induced birefringence must be taken into account. Second, the single-mode (SM) calculation is very important. If the stress effects are taken into account, the curve is modified. Here, the stress influence is higher for smaller values of etch depth. Third, we find the locus where both SM and ZBR conditions are fulfilled. In the isotropic case, the ZBR and SM curves do not overlap. If we consider the ZBR curve calculated by using stress-induced effects and the quasi-TM curve calculated in the isotropic case, we find that the curves are much closer, but still both SM and ZBR conditions cannot be satisfied. Only when the SM and ZBR curves are calculated for the anisotropic distribution of the refractive index can both conditions be satisfied. This again shows that the stress needs to be taken into account. In many ways, this is fortuitous result, as it means the stress allows us to fabricate small waveguides that satisfy both the SM and ZBR conditions. Figure 3(b) represents a similar situation to Figure 3(a), but for a waveguide with the slanted sidewalls of 80°. In the isotropic case, a relatively short locus that satisfies both SMC and ZBC is found, while in the anisotropic case, the desired locus is larger. It is also worth noting that the two SM curves are closer to each other for deeper ribs when θ=90° while the opposite is true when θ=80°. For vertical sidewalls and ribs with large values of D, the mode will reside mainly in the slab, and therefore, the influence of the oxide is reduced. Hence, the two SM curves in Figure 3(a) are similar for deeper ribs. If the sidewalls are slanted, then the difference between the top rib width and the bottom (and also effective) rib width increases with an increase in etch depth. Therefore, the influence of the oxide stress increases and hence the difference between the two SM curves in Figure 3(b) increases for larger D.

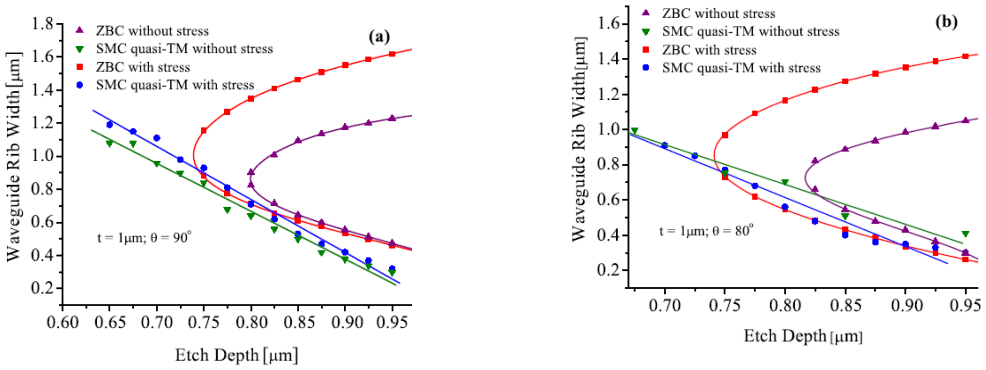

Figure 3. Single-mode and zero birefringence conditions for top oxide thickness and sidewall angle of (a) t = 1 μm, θ = 90° and (b) t = 1 μm, θ = 80° [12]

3. Filters

The consortium is currently exploring two types of filters, MMI based filters, and Ring resonators

3.1 MMI Based filters

This section describes a novel approach to wavelength filters, multiplexers and de-multiplexers in SOI waveguide technology. The approach is based on wavelength dependent self-imaging in rectangular cross-section multimode waveguides. The work builds on earlier studies of multimode interference (MMI) phenomena which are at the heart of the wavelength dependent self-imaging function. The underlying MMI phenomena have formed the basis of a very wider range of easily designed and easily manufactured integrated optic devices. These include: splitters, mixers, switches, modulators etc. As a consequence the realisation of wavelength filtering, multiplexing and demultiplexing functions would provide useful additional functionality to this particular set of devices. One form of the wavelength filtering, multiplexing and demultiplexing device to be considered is illustrated schematically in plan view in figure 4. In its simplest configuration it consists of fundamental mode input and output waveguides of cross-section a in conjunction with a multimode waveguide of height a and width b. The walls of the fundamental and multimode waveguides are at $\pm a/2$ and $\pm b/2$, respectively. As illustrated, the input waveguide is tilted with respect to the multimode waveguide axis by an angle θ and laterally offset from it such that the wall of the input waveguide at $+a/2$ coincides with the wall of the multimode guide at $+b/2$, i.e. the axis of the fundamental mode input guide intercepts the input plane of the multimode guide at a point $(b - a/\cos\theta)/2$ from the axis of the multimode guide.

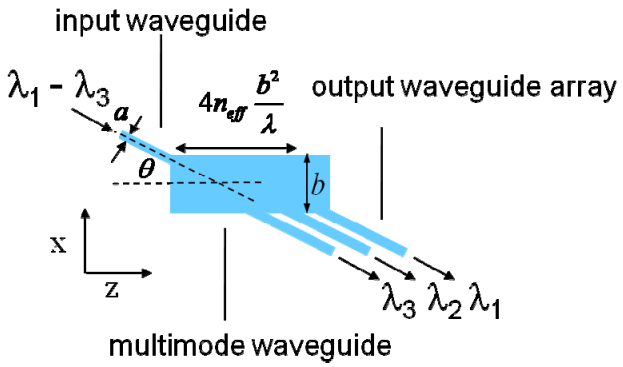

Figure 4. Schematic of plan view of filter and mux/demux concept based on wavelength dependent self-imaging in a rectangular multimode waveguide

In conjunction with the input waveguide configuration, as illustrated, an array of fundamental mode output guides are arranged on the opposite wall of the multimode guide with identical angular tilts with respect to the multimode waveguide axis. The axial positions of the centres of the waveguides in the output array are based on the wavelengths in the input spectrum that they are designed to capture. For example, the axial position of the output waveguide designed to capture the free-space wavelength λ is given by:

$$L = \frac{4n_{eff}b^2}{\lambda} \qquad (1)$$

Here, n_{eff} is the effective index of the fundamental *TE* mode of the planar waveguide associated with the specific epitaxial layer design that the device will be formed in. At the axial point L an inverted self-image of the fundamental mode input field is produced. Differentiating L in equation (1) with respect to λ yields:

$$dL = -4n_{eff}\left(\frac{b}{\lambda}\right)^2 d\lambda \qquad (2)$$

This predicts how the magnitude of the axial shift of the inverted self-image of the input field along the side wall of the multimode waveguide depends on the square of the ratio of the multimode guide width to the input wavelength. The negative sign indicates that as the input wavelength increases the self-imaging point moves towards the input plane. In order to clarify how a mux/demux device might operate in practice figure 5 shows predictions for a fixed input waveguide inclination of 0.1 rad but where the free-space input wavelength is changed in 50 nm steps from 1.5 µm to 1.7 µm. The predictions all relate to the output plane and illustrate how the self-image of the fundamental mode input field moves along the side wall of the multimode waveguide. Although only a qualitative conclusion at this stage, it is clear from figure 5 that effective coupling of the different wavelengths of the input field to different output waveguides in the output array should be feasible in practice.

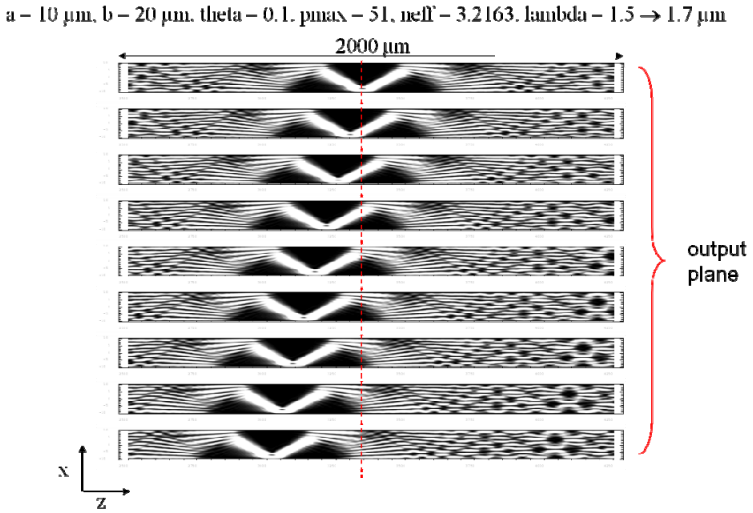

Figure 5. Theoretical plots of the transverse intensity in the multimode waveguide when the free-space input wavelength is incremented in 50 nm steps from 1.5 µm to 1.7 µm. The calculations indicate how the axial position of the self-image of the input field changes with wavelength.

In relation to figure 5, simple geometric considerations of the projection of the self-image of the fundamental mode field from the input waveguide onto the side wall of the multimode guide, coupled with the dispersion relationship provided by equation 2, leads to the following expression for the wavelength resolution:

$$d\lambda \approx -\frac{1}{4n_{eff}}\left(\frac{\lambda}{b}\right)^2 \frac{a}{\theta} \qquad (3)$$

This highlights how for a given free-space wavelength and epitaxial layer design, the choice of the input guide width and angle of inclination coupled with the multimode guide width define the wavelength resolution achievable in practice. The choice of these parameters and their impact on the total bandwidth

of a filter or mux/demux device and the number of resolvable wavelengths in the latter case will be consider in more detail in the next phase of the work.

3.2 Ring Resonators

Small ring resonators are well known optical filters. The simplest structure is a single resonator. It consists of a resonator and a straight waveguide acting as an input/output (through) port. A straight waveguide can be added to observe the spectrum at the second output also known as the drop port. Whilst single rib waveguide based resonators cannot give very large FSRs, typically up to a few nanometres, the devices based upon strip waveguides are capable of producing relatively large FSRs, over 10s of nm. Therefore, it is worth considering a single resonator structure. We have already previously demonstrated small optical filters with an FSR as large46nm [13], and 62nm [14] (Figs 6 & 7). In figure 6, the FSR is 46nm, the extinction ratio is measured to be 12.6, and FWHM is estimated to be ~3.1nm at 1540nm and ~5.5nm at 1586nm giving the values for the Q factor between 200 and 400 depending on the value for the group index.

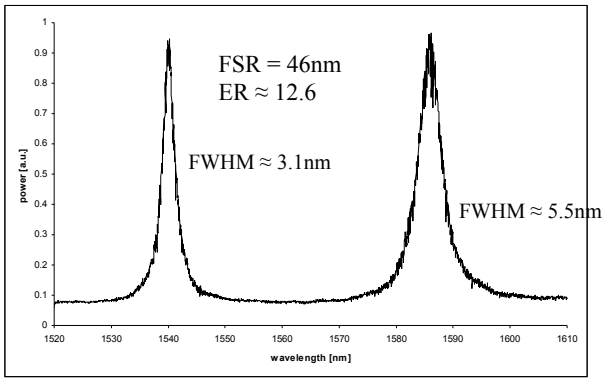

Fig. 6 TE response of a 2µm ring at the drop port.

Nevertheless, the FSR as large as 62nm has been obtained by using 1.5µm radius rings as it is shown in Fig. 7**.** The same figure depicts that stability of the response might be an issue. The second graph in Fig. 7 represents response of a similar device, where the same structure parameters have been used, but from a different test chip for which slightly different exposure recipes were utilised during the lithography process in order to fabricate target devices. It can be seen that the FSR is not affected, but a shift of ~9nm has been introduced. Considering that the modes are very likely to react differently to the change, polarisation insensitivity can be significantly altered. Thus, very accurate waveguide and device layouts are prerequisite for stable response and good control over the polarisation properties.

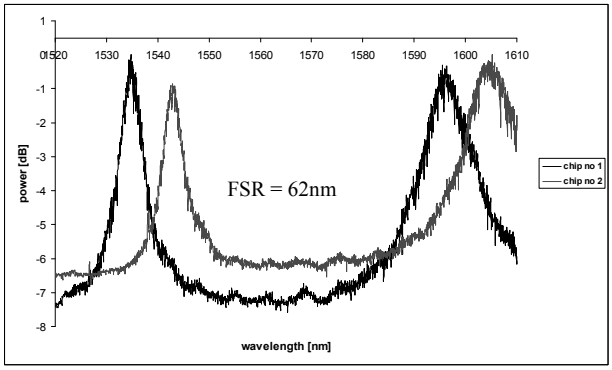

Fig. 7 The responses of 1.5µm rings with identical parameters to those used in figure 6 but slightly differen lithography exposure. The resonators are made of waveguides which width is 380nm and height 290nm. Th obtained FSR is ~62nm.

4. Modulators

The project is contributing to work on optical modulators in 3 areas: Conventional waveguide modulators, photonic crystal modulators, and Quantum Confined Stark Effect (QCSE) modulators. These will be discussed in turn:

4.1 Conventional modulators

In order to increase the bandwidth further, a sub-micrometer modulator based on the depletion of a p-n junction was proposed in 2005 by Gardes *et al*. The depletion type phase shifter is not limited by the minority carrier recombination lifetime and is based on the principle of removing carriers from the junction area when applying a reverse bias. Figure 8 shows a four terminal asymmetric pn structure,

where the concentration of *n*-type doping is much higher than the concentration of *p*-type doping. The reason for such a structure is firstly to minimize the optical losses induced by the *n*-type doping and secondly to enhance the depletion overlap between the optical mode and the *p*-type region, in order to induce a better phase shift to length ratio.

The carrier concentration variation in this kind of device is not uniform, as can be seen in the predictions of the refractive index change in the waveguide shown in Figure 9, and arises on both sides of the junction over a width of around 200 nm. One way to optimize the device is by increasing the overlap between the optical mode and the *p*-type depleted region. The main advantage of using depletion is obviously the very fast response time, simulated to be 7 ps for this modulator. This corresponds to an intrinsic bandwidth of approximately 50 GHz, although this takes no account of contact resistance nor electrode influence. The device proposed by Gardes et al was 2.5 mm long and operated with a reverse bias swing of 5 Volts in a push-pull configuration as part of a Mach Zehnder interferometer (MZI).

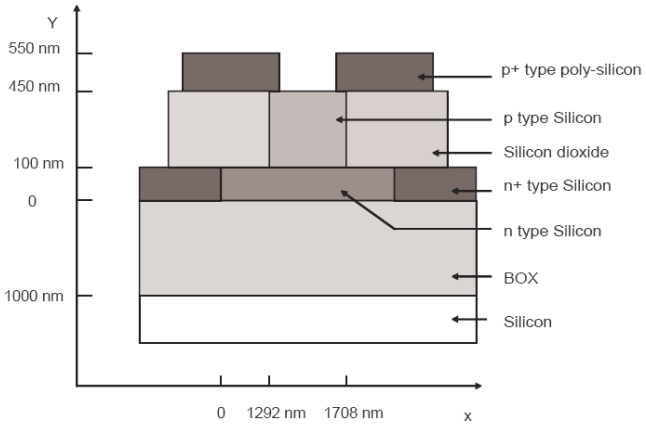

Figure 8: Schematic of a four terminal depletion type modulator [15]

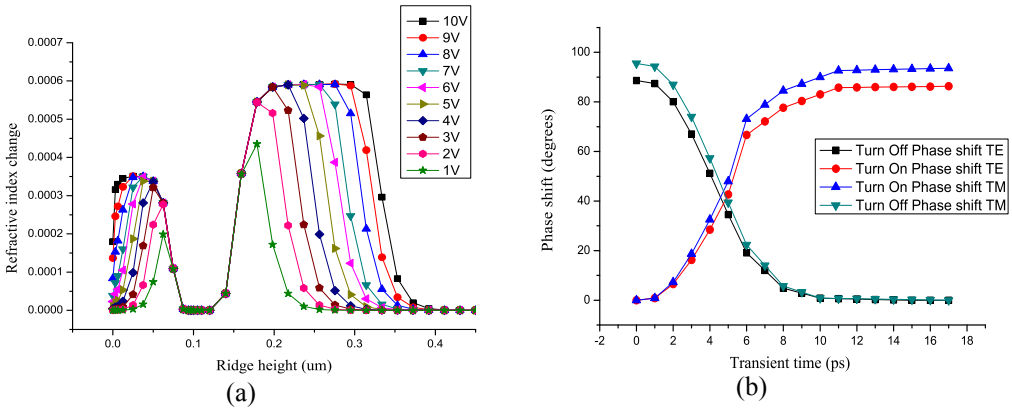

Figure 9: (a)Variation of refractive index in the waveguide. (b)Rise and fall time for TE and TM [15]

To improve further compactness and simplify fabrication a modulator based on a depletion of a vertical pn junction was demonstrated by Gardes et al. [16] . The proposed ring resonator modulator is based on a 300 nm wide, 150 nm etch depth and 200 nm high rib waveguide, which enables single mode transmission. As shown in Fig. 10, the pn junction is asymmetrical in size and in doping concentration in order to maximize the area of hole depletion that overlaps with the optical mode. The n-type region is 75 nm wide and the p type 225 nm wide, and the net doping concentration of this particular junction varies between 6 x 10^{17}.cm^{-3} and 2 x 10^{17}.cm^{-3}, for n and p types, respectively. The junction was fabricated using ion implantation at CEA Leti in France, and the Ion Beam Centre at the University of Surrey.

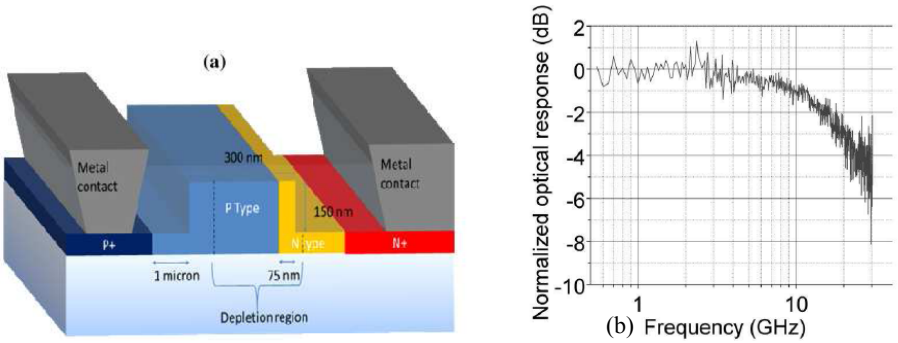

Figure 10: (a) Modulator schematic. (b) Frequency response[16]

The modulator exhibited a DC on/off ratio of 5 dB at -10 V, and a 3 dB bandwidth of 19 GHz. despite the relatively high bandwidth result, the device is non-optimal, which can be attributed to misalignment of the junction and incomplete activation of the dopants used to form the pn junction.

We are currently working on two additional optical phase modulator designs as part of two different projects. The first is funded via the European Union Framework as part of a project known as HELIOS, and the second is part of this project, funded by the Engineering and Physical Sciences Research Council (EPSRC). In both cases the aim is to demonstrate modulator variants with speeds of 10Gb/s and 40Gb/s.

4.2 Photonic Crystal modulators

To achieve a modulator with simultaneously a low footprint and broad bandwidth, we placed dispersion-engineered photonic crystal waveguides [17] in each arm of a symmetric Mach-Zehnder interferometer, as shown in fig. 11. The design group index of the photonic crystal was 28, enhancing the phase change by almost a factor of 10. The phase shift is provided via the thermo-optic tuning of one of the arms by means of an integrated microheater. The entire structure is clad with silica, (the cross-section is presented in fig. 11b), which, although reducing the index contrast, improves the CMOS compatibility. It also provides a spacer layer to isolate the optical mode from the lossy metal of the microheaters. The reduced refractive index contrast introduces some additional design limitations, slightly reducing the group indices achievable relative to air-bridge versions, but crucially, the loss per unit delay is not increased [18].The fabrication closely follows that of [18] and [19]. The photonic crystal pattern is created in a Silicon-on-Insulator wafer with a 220nm top silicon layer on a 2μm of buried oxide. Silica cladding is then deposited using the spin-on-glass FOx-14 (commercially available from Dow-Corning). A nickel microheater, consisting of 5μm wide, 80nm thick strips of nickel, is then added over one of the PhC phase-shifters using a photo-lithography, evaporation deposition, and lift-off procedure. A micrograph of the final device is shown in figure 11.

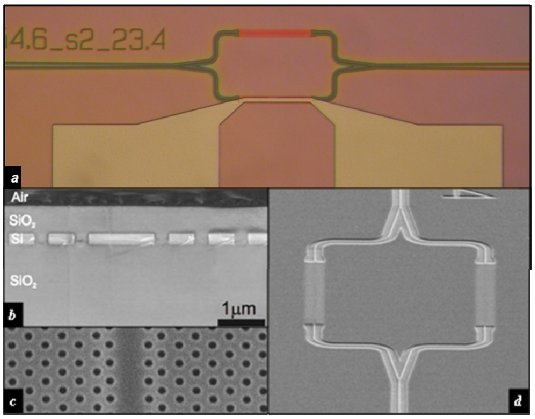

Figure 11(a) An optical micrograph of the finished device. (b) An SEM micrograph of the cross-section of the oxide clad PhC. (c) A close-up of the waveguide. (d) An overview of the complete Mach Zehnder

As silicon has a thermo-optic coefficient of $dn/dT = 1.8 \times 10^{-4} K^{-1}$, its refractive index increases with temperature. When the microheater is on, the dispersion curve of the photonic crystal waveguide mode is shifted to lower frequencies, changing the k-vector and thus inducing a phase-shift between the two arms. When this phase shift, ΔkL, reaches a value of π, the light propagating in each arm of

the Mach Zehnder interferometer destructively interferes at the output, switching the device to its off state. The slow-light enhancement is now apparent- a greater phase shift per unit length of the waveguide is achieved, allowing the physical length of the device to be reduced (whereas the optical length is constant).
When heat is applied, the shift in wavevector is given by $\Delta k = \Delta n\ \omega_0\ S$, where $S = n_g/n$ is the slow-down factor, Δn is the change of refractive index and ω_0 is the frequency. The length required for the π phase shift is reduced by a factor S. To give figures for the example shown here, a phase-shifter 80μm long is required to operate with an index change of approximately 10^{-3}.

Fig. 12b shows the transmission of the MZI at a wavelength in the middle of the flatband slowlight region (1581nm) as a function of the thermal heating. It should be noted that the first peak in transmission occurs at a power of approximately 9mW, indicating that the MZI is initially slightly unbalanced. This unbalancing is due to fabrication imperfections meaning that the arms are not quite perfectly equal in length, or that the metal for the heater slightly disturbs the optical mode. The power required to achieve the π phase change needed to switch the modulator from on to off is 17mW, and the measured modulation depth is an impressive 20dB. Fig. 12 (a) also demonstrates the broadband nature of the modulator design-modulation with an extinction ratio in excess of 15dB is obtained over a bandwidth of 11nm (calculated from the average transmission over this bandwidth). This is a striking contrast to the very limited bandwidth offered by ring resonator modulators.

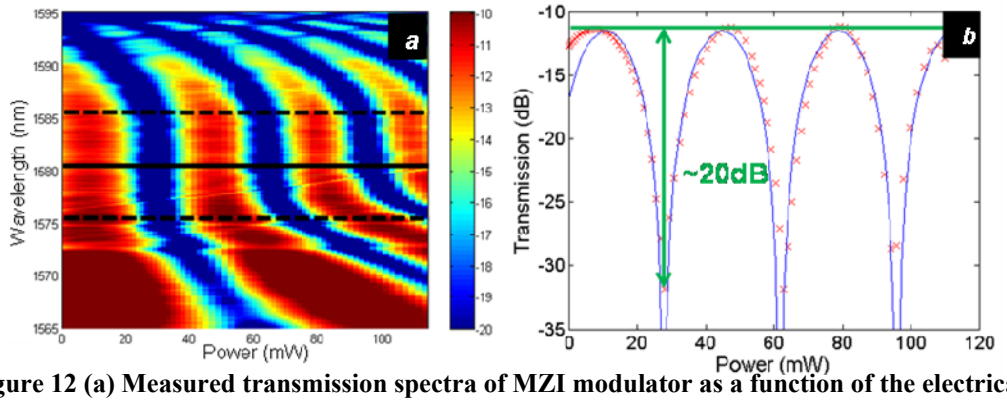

Figure 12 (a) Measured transmission spectra of MZI modulator as a function of the electrical power delivered to the integrated microheater. The dashed lines represent the limits of the 11 nm bandwidth. The colour bar gives the transmission in decibels. (b) Measured (red crosses) and calculated (blue lines) transmission at 1581 nm, as marked by the solid line in (a).

4.3 Quantum Confined Stark Effect Modulators

Carrier accumulation or depletion type Mach-Zehnder modulators tend to be several millimeters in length and dissipate considerable amounts of power [20]. As such, there exists the need to develop compact low-power modulators. The quantum-confined Stark effect (QCSE) describes a shift in the absorption edge of a quantum-well heterostructure under the application of an external field. This shift can be exploited in electroabsoprtion (EA) devices, and has been used to fabricate compact high-speed waveguide-integrated devices that can be monolithically integrated with semiconductor lasers in III-V systems [21-23].

Ge/SiGe heterostructures can be epitaxially grown on Si substrates using reduced-pressure chemical vapour deposition (RP-CVD). There is a 4.2% lattice mismatch between Si and Ge, and this means that at least one of the layers in the multiple-quantum-well (MQW) stacks will be strained. Furthermore, to be mechanically stable, the MQW stack should be strain symmetrized to a relaxed SiGe *virtual substrate*, or *buffer*, where the strain is relieved via misfit dislocations near the Si/SiGe interface. In such a system, the Ge quantum wells will be compressively strained and the SiGe barriers will be tensile strained, and zero

net strain is accumulated for each well/barrier pair, so several quantum wells can be grown in a single heterostructure.

The QCSE in Ge/SiGe MQW systems was first demonstrated in 2005 [24], where a contrast in the absorption coefficient of a factor of 4.69 was reported at ~1450 nm. Many fibre-optic telecommunications systems exploit the spectral 'window' at 1310 nm, which corresponds to the zero dispersion in standard single-mode fibres. Passive optical network architectures typically use 1310 nm for upstream signals [25], and so compact, low-cost and low-power modulators operating at 1310 nm that can be integrated into Si electronic-photonic integrated circuits would be extremely desirable for emerging fibre-to-the-home applications. Here we describe designs for MQW heterostructures where strain engineering was employed to target EA modulation at 1310 nm.

A combined 6×6 **k.p** and one-band effective mass model was used to calculate the hole and electron wavefunctions, respectively, details of which can be found in [26]. Hydrostatic strain was incorporated into the model using model solid theory and light-hole/heavy-hole splitting due to uniaxial strain was included in the **k.p** Hamiltonian. Optical absorption occurs in the Ge quantum wells, and the absorption edge is determined by the (direct) Γ bandgap, even though Ge has an indirect bandgap since the indirect absorption is very weak. The strain in the Ge quantum wells is determined by the compostion of the virtual substrate, as the epitaxial layers will be lattice matched to it. As the Si fraction of the virtual substrate increases, the Ge layers experience increasing levels of compressive strain. Compressive strain increases the Γ bandgap, shifting the absorption edge to shorter wavelengths.

Our device uses 8-nm Ge quantum wells grown on a $Si_{0.25}Ge_{0.75}$ virtual substrate, and strain symmetrisation is achieved using 11-nm-thick barriers. The simulated absorption spectra at several electric fields are shown in Fig. 13. A contrast in the absorption coefficient of a factor of approximately six is observed at 1310 nm between zero field and an electric field of 220 kV/cm. In order to examine the expected performance of a waveguide integrated device, we calculated the fundamental mode profile of a vertically-coupled waveguide-integrated mesa device. A 400-nm-thick SOI substrate with a 500-nm-thick SiGe *p*-type virtual substrate layer was modelled (consistent with the device in [24], together with two 50-nm-thick intrinsic spacer layers surrounding ten quantum wells, with a 50-nm-thick *n*-type top contact layer. We find that there is a 25% modal overlap with the MQW active region of the device. (This can be increased if a thinner virtual substrate is used, however, this has implications for the quality of the growth). Using the absorption coefficients in the on- and off-states of the MQW structure, together with the modal overlap, and assuming that there is no coupling loss and absorption only occurs in the MQW region, we can readily calculate the expected attenuation of a signal as it propagates through the structure. We find an extinction ratio of 14 dB and an insertion loss of 3 dB for a 25-μm-long device.

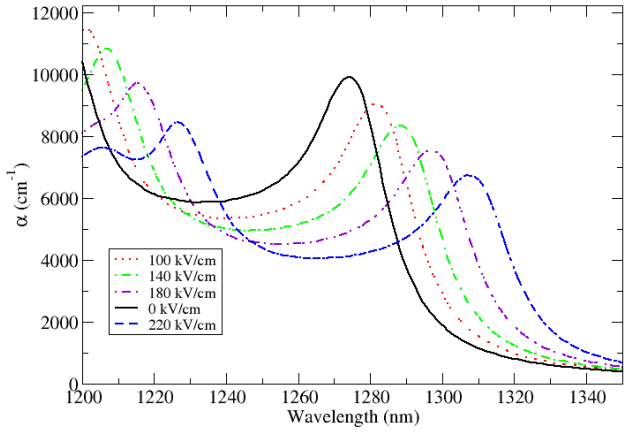

Figure 13 Absorption spectra at different electric fields. At 1310 nm the simulated absorption coefficient, α, is 1,100 cm^{-1} with no field, and is 6,500 cm^{-1} under and applied field of 220 kV/cm.

5. Raman Amplifiers

The Raman effect has been used successfully to produce a silicon laser [27], however very high intensity pump lasers are required to generate amplification due to a non-linear effect known as two-photon-absorption (TPA) [28] which causes free-carrier absorption (FCA) loss that can exceed Raman gain as well as depleting pump photons. Integrated p-i-n diodes have been used previously to remove these carriers, and hence reduce the effective carrier lifetime. However they appear less effective at high powers due to carrier screening of the reverse bias voltage [29,30]. Scaling the waveguide to sub-micrometer sized dimensions can reduce the effective lifetime of carriers due to enhanced surface recombination [31,32], however in that case the problem of high coupling losses has to be addressed.

It has already been shown that implanting helium into rib waveguides [33] can reduce the carrier lifetime without a drastic increase in propagation loss. A net Raman gain of 0.065dB was measured in that case without the need for a reverse bias diode to remove the photo-generated free carriers.

The work in this paper is based on the implantation of silicon**.** We discuss the use of ion induced defects to trap the carriers generated from the TPA process, and the effect of the implanted defects on propagation inside the waveguide. The depth of the defects in the waveguide and their concentration is varied to investigate the effect this has on free carrier lifetime and excess optical absorption. Modelling has shown that high gain is possible for a device not containing an electric field, if a low effective carrier lifetime can be achieved with no increase in propagation loss [29]. Here we show that the introduction of a thin defect layer at the waveguide surface produces this scenario. Silicon ion implantation is a process now used commonly in the fabrication of CMOS type devices, for example in the creation of shallow amorphous layers. Further use of such self ion implantation prevents any possibilities of modification via chemical doping effects. Previous studies of defects created via self irradiation of silicon are substantial in volume and thus significant data is available to those wishing to model the recombination characteristics of defect engineered structures.

5.1 Experimental method and results

Silicon rib waveguides were fabricated on a (100) silicon-on-insulator (SOI) wafer. The rib dimensions were nominally width 1μm and height 1.35μm. The waveguides had a length of 8000μm.

Ion implantation modeling was carried out using ATHENA [34] to find the damage range in relation to the rib waveguide cross sectional dimensions. Ion implantation energies were chosen to provide a range of damage depths in the rib waveguide. This varied from near-surface implantation range to fully implanted waveguides.

Measurement of propagation loss was made in a manner similar to that employed by Foster et al. using a broadband source with a wavelength range of 1530nm to 1610nm [35]. Implant windows varied in length from 0μm to 8000μm increasing in steps of either 1000μm or 2000μm.

Figure 14 shows excess loss introduced by ion implantation versus dose, for different implantation energies. As dose increases, so does the excess loss introduced to the waveguide. Excess loss also increases with implantation energy (for a given dose), until the highest energy of 2000keV, at which point the peak of the asymmetric damage profile passes through the SOI device and is positioned in the buried oxide below.

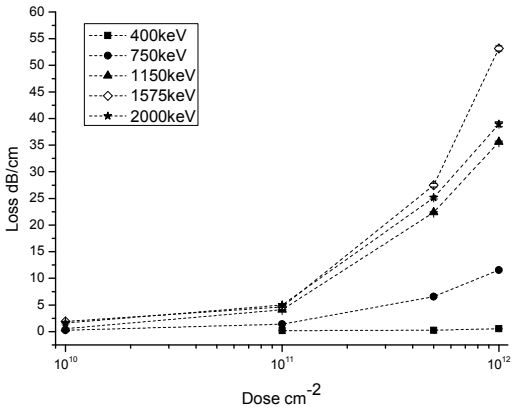

Fig. 14. Experimental data of excess loss versus dose for different silicon implantation energies

The experimental setup for carrier lifetime measurements required the addition of a femto-second pulsed laser directed onto the top of the waveguide. Figure 15 shows a diagram of the measurement technique. The broadband source used previously to measure propagation loss, is now used as the probe beam in this experiment, with a

maximum power available of ~4mW. The pump beam had a pulse width ~80fs.

Directing the pump beam from above onto the waveguide being measured, allowed both implanted and un-implanted regions to be measured using near identical experimental conditions. This approach is similar to the one used by Waldow et. al, to investigate argon and oxygen implantation on switching speeds in silicon microring resonators [36]. The penetration depth with a wavelength of 800nm in silicon is much larger than the waveguide height in this experiment [37]; hence a distribution of carriers will exist throughout the waveguide which will behave in the same manner as those generated by the co-linear approach [38].

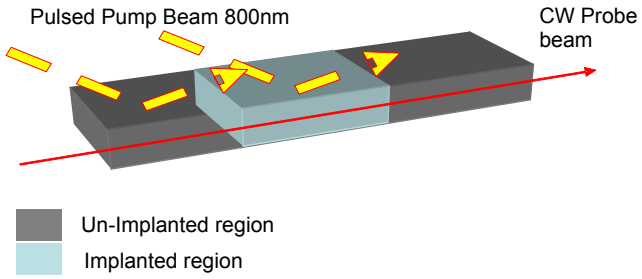

Fig. 15. Free carrier lifetime measurement technique. The laser is aligned with the top of the waveguide. This excites carriers which attenuate the broadband beam. During the off-cycle of the pump the carriers recombine.

The largest reduction in lifetime was 94.47%; corresponding to a carrier lifetime of 0.23ns. However the excess loss introduced into the waveguide for this implantation was unacceptably high ~22.38dB/cm. In comparison, utilizing the lowest ion implantation energy yields an 85.4% reduction in lifetime corresponding to ~0.56ns, for only ~0.54dB/cm excess loss. Figure 16 displays excess loss data for the 400keV implantation together with the percentage reduction in free carrier lifetime, as a function of ion dose. The carrier lifetime for each corresponding dose is also shown.

This work has shown that silicon ion implantation is successful at reducing the free carrier lifetime of a silicon waveguide. Low energy silicon implantation provides the best compromise between excess linear loss and reduction in free carrier lifetime, due to little or even zero modal overlap between the damage and the propagating signal. It should be noted that the procedure of implantation to modify carrier lifetime would be best utilized as a back end process due to the fact that damage introduced by low dose Si ions, anneals out at ~350°C [35]. It should be noted however, that this is also true for any low dose ion implantation process such as those discussed for other ion species.

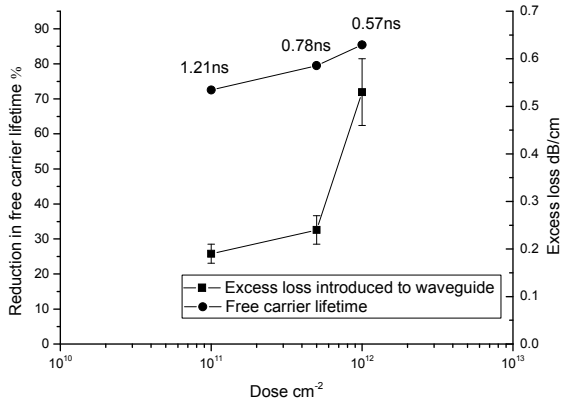

Fig. 16. Plot comparing excess loss and reduction in free carrier lifetime for 400keV energy with 10^{11}, $5x10^{11}$ and $10^{12}cm^{-2}$ doses. As the concentration (ion implantation dose) of defects increases so does the excess loss and reduction in free carrier lifetime.

6. Conclusion

The UK Silicon Photonics work is active in a variety of areas concerning the development of silicon photonics. Work is progressing well, and some of the work has been reported here, although it is impossible to give a comprehensive review in an overview paper. All areas are working towards demonstrators devices that incorporate electronic and photonic integration, whilst maintaining excellent performance for individual devices. It is anticipated that detailed results will be published in the near future.

7. Acknowledgements

This work has been funded by the Engineering and Physical Sciences Research Council (EPSRC) programme, "UK Silicon Photonics". The authors are grateful to EPSRC for funding this work.

8. References

1. R A Soref, S J Emelett and W R Buchwald 2006 *J. Opt. A: Pure Appl. Opt.* **8** 840
2. Raghunathan V, Borlaug D, Rice R R and Jalali B *Proc. LEOS 4th Group IV Photonics*, Tokyo, Japan, PD2, 2007.
3. M. Koshiba, K. Kakihara and K. Saitoh, "Reduced lateral leakage losses of TM-like modes in silicon-on-insulator ridge waveguides," Opt. Lett., 33(17), 2008-2010 (2008).
4. L. K. Rowe, M. Elsey, N. G. Tarr, A. P. Knights, and E. Post, "CMOS-compatible optical rib waveguides defined by local oxidation of silicon," *Electronics Letters,* vol. 43, pp. 392-393, 2007.
5. F. Y. Gardes, G. T. Reed, A. P. Knights, G. Mashanovich, P. E. Jessop, L. Rowe, S. McFaul, D. Bruce, N. G. Tarr, "Submicron optical waveguides for silicon photonics formed via Local Oxidation of Silicon (LOCOS)," Proc. SPIE 6898-23 (2008).
6. www.photondesign.com
7. M. A.Webster, R. M. Pafchek, A. Mitchell and T. L. Koch, "Width dependence of inherent TM-mode lateral leakage loss in silicon-on-insulator ridge waveguides," IEEE Photon. Technol. Lett., 19(6), 429-431 (2007).
8. M. Koshiba, K. Kakihara and K. Saitoh, "Reduced lateral leakage losses of TM-like modes in silicon-on-insulator ridge waveguides," Opt. Lett., 33(17), 2008-2010 (2008).
9. R. M. Pafchek, J. Li, R. S. Tummidi, and T. L. Koch, "Low loss Si-SiO_2-Si 8-nm slot waveguides," IEEE Photon. Technol. Lett., 21(6), 353-355 (2009).
10. T. G. Nguyen, R. S. Tummidi, T. L. Koch, and A. Mitchell, "Rigorous modeling of lateral leakage loss in SOI thin-ridge waveguides and couplers," IEEE Photon. Technol. Lett., 21(7), 486-488 (2009).
11. Ye W N, Xu D-X, Janz S, Cheben P, Picard M-J, Lamontagne B and Tarr N G 2005 *J. Lightwave Technol.* **23** 1308.
12. M. Milosevic, P. Matavulj, B. D. Timotijevic, G. T. Reed, and G. Z. Mashanovich, "Design rules for single mode and polarization independent silicon-on-insulator rib waveguides using stress engineering," *J. Lightwave Technol.*, vol. 26, pp. 1840 – 1846, 2008.
13. B. D. Timotijevic, G. T. Reed, R. Jones, A. Michaeli, A. Liu, and G. Z. Mashanovich, "Small optical filters in silicon-on-insulator", 3rd Int. Conf. Group IV Photonics, , pp. 25-27, Ottawa, Canada, 2006.
14. B. D. Timotijevic, D. Thomson, F. Y. Gardes, S. Howe, A. Michaeli, R. Jones, J. V. Crnjanski, V. M. N. Passaro, G. Z. Mashanovich, and G. T. Reed, "Tailoring the response and temperature characteristics of multiple serial-coupled resonators in silicon on insulator," Proc. SPIE, vol. 6447, 2007.
15. F. Y. Gardes, G. T. Reed, N. G. Emerson, and C. E. Png, "A sub-micron depletion-type photonic modulator in silicon on insulator," *Optics Express,* vol. 13, 2005.
16. F. Y. Gardes, A. Brimont, P. Sanchis, G. Rasigade, D. Marris-Morini, L. O'Faolain, F. Dong, J. M. Fedeli, P. Dumon, L. Vivien, T. F. Krauss, G. T. Reed, and J. Martí, "High-speed modulation of a compact silicon ring resonator based on a reverse-biased pn diode," *Opt. Express,* vol. 17, pp. 21986-21991, 2009.
17. J. Li, T. P. White, L. O'Faolain, A. Gomez-Iglesias, and T. F. Krauss, "Systematic design of flat band slow light in photonic crystal waveguides," Optics Express, vol. 16, pp. 6227–6232, 2008.

18. T. P. White, L. O'Faolain, J. Li, L. C. Andreani, and T. F. Krauss, "Silica-embedded silicon photonic crystal waveguides," Optics Express, vol. 16, pp. 17 076–17 081, 2008.
19. D. M. Beggs, T. P. White, L. Cairns, L. O'Faolain, and T. F. Krauss, "Ultrashort photonic crystal optical switch actuated by a microheater," IEEE Photonics Technology Letters, vol. 21, p. 24–26, 2009.
20. Liu, J., et al., "Waveguide-integrated, ultralow-energy GeSi electro-absorption modulators*",* Nat Photon, 2008. **2**(7): p. 433-437.
21. Wood, T.H., *"*Multiple quantum well (MQW) waveguide modulators*",* Lightwave Technology, Journal of, 1988. **6**(6): p. 743-757.
22. Ido, T., et al., "MQW electroabsorption optical modulator for 40 Gbit/s modulation", Electronics Letters, 1995. **31**(24): p. 2124-2125.
23. Lewén, R., et al., "Segmented Transmission-Line Electroabsorption Modulators", J. Lightwave Technol., 2004. **22**(1): p. 172.
24. Kuo, Y.-H., et al., "Strong quantum-confined Stark effect in germanium quantum-well structures on silicon*",* Nature, 2005. **437**: p. 1334-1336.
25. Lam, C., "Passive Optical Networks: Principles and Practice",2007.
26. Lever, L., et al. "Design of Ge/SiGe quantum-confined Stark effect modulators for CMOS compatible photonics", in *Silicon Photonics V*. San Francisco, California, USA: SPIE.
27. H. Rong, R. Jones, A. Liu, O. Cohen, D. Hak, A. Fang, M. Paniccia, "A continuous-wave Raman silicon laser," Nature. **433** 725-728 (2005).
28. R. Claps, V. Raghunathan, D. Dimitropoulos, B. Jalali, "Influence of nonlinear absorption on Raman amplification in Silicon waveguides," Opt. Express **12** 2774-2780 (2004).
29. D. Dimitropoulos, D. R. Solli, R. Claps, O. Boyraz, B. Jalali, "Noise figure of silicon Raman amplifiers," J. Lightwave. Tech. **26** 847-852 (2008).
30. D. Dimitropoulos, S. Fathpour, B. Jalali, "Limitations of active carrier removal in silicon Raman amplifiers and lasers," Appl. Phys. Lett. **87** 261108 1-3 (2005).
31. R. L. Espinola, J. I. Dadap, R. M. Osgood, Jr., S. J. McNab, Y. A. Vlasov, "Raman amplification in ultrasmall silicon-on-insulator wire waveguides," Opt. Express **12** 3713-3718 (2004).
32. D. Dimitropoulos, R. Jhaveri, R. Claps, J. C. S. Woo, B. Jalali, "Lifetime of photogenerated carriers in silicon-on-insulator rib waveguides," Appl. Phys. Lett **86** 071115 1-3 (2005).
33. Y. Liu, H. K. Tsang, "Nonlinear absorption and Raman gain in helium-ion-implanted silicon waveguides," Opt. Lett. **31** 1714-1716 (2006).
34. Silvaco International, 4701 Patrick Henry Drive, Bldg 1, Santa Clara, CA 94054, www.silvaco.com
35. P.J.Foster, J.K.Doylend, P.Mascher, A.P.Knights, P.G.Coleman, "Optical attenuation in defect-engineered silicon rib waveguides", J. Appl. Phys. **99**, 073101 1-7 (2006).
36. M. Waldow, T. Plötzing, M. Gottheil, M. Först, J. Bolten, T. Wahlbrink, and H. Kurz, "25ps all-optical switching in oxygen implanted silicon-on-insulator microring resonator," Opt. Express **16**, 7693-7702 (2008)
37. M. Y. Shen, C. H. Crouch, J. E . Carey, R. Younkin, E. Mazur, M. Sheehy, C. M. Friend, "Formation of regular arrays of silicon microspikes by femtosecond laser irradiation through a mask," Appl. Phys. Lett. **82** 1715-1717 (2003)
38. A. Liu, H. Rong, R. Jones, O. Cohen, D. Hak, M. Paniccia, "Optical amplification and lasing by stimulating raman scattiering in silicon waveguides," J. Lightwave. Tech. **24,** 1440-1455, 2006